



Heriot-Watt University  
Research Gateway

## Using infrared thermography to investigate thermomagnetic convection under spatial non-uniform magnetic field

### Citation for published version:

Szabo, P, Bekovic, M & Fruh, W-G 2017, 'Using infrared thermography to investigate thermomagnetic convection under spatial non-uniform magnetic field', *International Journal of Thermal Sciences*, vol. 116, pp. 118-128. <https://doi.org/10.1016/j.ijthermalsci.2017.02.004>

### Digital Object Identifier (DOI):

[10.1016/j.ijthermalsci.2017.02.004](https://doi.org/10.1016/j.ijthermalsci.2017.02.004)

### Link:

[Link to publication record in Heriot-Watt Research Portal](#)

### Document Version:

Peer reviewed version

### Published In:

International Journal of Thermal Sciences

### General rights

Copyright for the publications made accessible via Heriot-Watt Research Portal is retained by the author(s) and / or other copyright owners and it is a condition of accessing these publications that users recognise and abide by the legal requirements associated with these rights.

### Take down policy

Heriot-Watt University has made every reasonable effort to ensure that the content in Heriot-Watt Research Portal complies with UK legislation. If you believe that the public display of this file breaches copyright please contact [open.access@hw.ac.uk](mailto:open.access@hw.ac.uk) providing details, and we will remove access to the work immediately and investigate your claim.

# Using infrared thermography to investigate thermomagnetic convection under spatial non-uniform magnetic field

Peter S. B. Szabo<sup>a</sup>, Miloš Beković<sup>b</sup>, Wolf-Gerrit Früh<sup>a</sup>

<sup>a</sup>*School of Engineering and Physical Science, Heriot-Watt University, Riccarton, Edinburgh, EH14 4AS, United Kingdom*

<sup>b</sup>*Faculty of Electrical Engineering and Computer Science, University of Maribor, Slovenia*

---

## Abstract

Thermomagnetic convection was investigated experimentally by infrared thermography and validated numerically by a finite-element analysis. A cavity filled with a magnetic liquid was under the influence of a permanent magnet that provided an external magnetic field and was subjected to thermal forcing by maintaining the two opposite horizontal walls at different temperatures. All configurations were chosen to explore situations where the Kelvin body force and buoyancy would either oppose each other or act perpendicular to each other. As both body forces depend on temperature, the aim was to explore the degree by which heat transfer may be enhanced by only varying the temperature difference. The results demonstrate that the Kelvin body force, which can be much stronger than buoyancy, leads to convective flow where only conduction would occur without the presence of the magnet. An effective force ratio,  $r$ , is developed which suggests that an increase in temperature difference across the cavity initially leads to a dominance of thermomagnetic forcing over buoyancy but that the overall force balance becomes more moderate at higher temperature differences. The global effect of both body forces on heat transfer was characterised by the Nusselt number and a suitable modified Rayleigh number.

*Keywords:* Magnetic fluid, thermomagnetic convection, Kelvin body force, magnetic Rayleigh number

---

## 1. Introduction

Low thermal conductivity in conventional heat transfer fluids such as oil, water and ethylene glycol are a primary limitation for the development of energy efficient heat transfer that is required in many industrial applications. The capability to produce suspensions by adding nanoparticles with higher thermal conductivity, such as ferromagnetic fluids, enables a new class of heat transfer fluids [1]. A great advantage of using such fluids is not only the enhancement in thermal conductivity but also the magnetic response of the fluid that may additionally be used to create a thermomagnetically induced convective flow. Some of their applications and properties are given by [2, 3].

Ferromagnetic fluids are industrial colloidal suspensions of single domain magnetic particles with an equivalent diameter of approximately 10 nm. The particles are coated with a dispersant to prevent agglomeration and coagulation by maintaining an adequate spacing between magnetic particles. This provides colloidal stability when the particles are dispersed in a carrier fluid such as water, kerosene or a silicone based fluid. As a result, the magnetic particles follow Brownian motion while the macroscopic fluid behaves as a homogeneous magnetisable fluid [3, 4]. Here we have investigated the flow structure of thermomagnetic convection using infrared thermal imaging and comparing this to the results of a finite-element model of the experiment.

### 1.1. Thermomagnetic convection

Thermomagnetic convection refers to convective heat transfer based on a temperature gradient within a magnetic fluid that induces local variation in the fluid's magnetisation in the presence of a magnetic field. A key feature is the temperature dependence of fluid magnetisation: thus, cooler fluid is more magnetised than hotter fluid, resulting in a magnetisation gradient imposed by temperature differences that establish flow fields where cooler fluid moves towards higher magnetic field intensity and creates convection [5, 6, 7]. The resulting thermomagnetic convection may be controlled by varying the magnetic properties of the fluid, the temperature distribution and the applied magnetic field [8].

Thermomagnetic instabilities in spatially non-uniform magnetic fields were first obtained analytically in the early 1970s by Curtis [9] and accompanied by Lalas and Carmi [10]. Since then, the literature has grown, and thermomagnetic convection with the use of permanent magnets that comply with Maxwell's equation of electromagnetism was analysed by Ganguly et al. [6], Mukhopadhyay et al. [11] and Banerjee et al. [12]. Since then, natural and thermomagnetic convection has been studied in several geometries such as tubes [13], cylinders [14, 15], cavities [16, 17, 18] and in geosciences [19]. A systematic experimental investigation of combined natural and thermomagnetic convection in a cube subjected to a magnetic field from a permanent magnet was performed by Sawada et al. [20]. Snyder et al. [21] complemented these

---

*Email address:* P.Szabo@hw.ac.uk (Peter S. B. Szabo)

experiments with a computational simulation for the same configurations but approximating the magnetic field through a constant gradient. While the simulations were able to reproduce single convection cells for natural convection and for convection with strong magnets, their model could not reproduce the two-cell flow structures suggested by the experimental observations.

In this study, we follow the approach taken by Sawada et al and Snyder et al. but, instead of investigating the effect of thermomagnetic convection on natural convection on a fluid with an imposed horizontal temperature gradient, we consider a stably stratified fluid cooled from below and heated at the top. By choosing this particular configuration, the focus is not on how thermomagnetic convection can be used to enhance natural convection. Instead, the focus is on how thermomagnetic convection can act as a substitute for natural convection and how this process can be studied in an Earth-based laboratory as was proposed by Fröh [19] albeit for a different purpose and context.

For the computational simulations complementing and validating the experiments, we chose not to approximate the magnetic field with a constant field gradient [21] or with an analytical solution [6, 12] but to solve the magnetostatic equations within the same finite-element package as the governing equations for the heat and fluid flow.

Finally, we present infrared thermography as an alternative non-invasive technique to observe the solution structure in the fluid.

### 1.2. Infrared thermography for heat and fluid flow

As magnetic liquids are opaque, it is challenging to visualise the flow structures in them. Up until now, the measurements of fluid velocities in a magnetic fluid have been restricted to in-situ sensors, such as hot-film anemometry [22], or non-invasive velocity measurements such as Ultrasound Doppler velocimetry [23] or, in the case of very thin layers, micro-PIV [24]. In addition to local temperature probes, such as thermistors or thermocouples [25, 16], liquid-crystal thermography has been explored to measure the temperature field in cubic enclosures [26, 27, 28] and a Hele-Shaw cell [29, 30], where one side of the cell was sprayed with a temperature sensitive liquid crystal. An alternative to liquid-crystal thermography is infrared thermography whereby the temperature of an object is visualised using an infrared camera. Thermal imaging of a fluid's temperature field is easily accomplished in convection experiments with a free surface [31].

Here we present a visualisation of the temperature field in the fluid cavity through one of the cavity walls made of thin perspex. As perspex absorbs most of the thermal infrared radiation, the visualisation is in fact that of the perspex surface whose temperature reflects that of the fluid through heat conduction. However, as will be demonstrated below, the perspex temperature field reflects that of the fluid, at least on length scales similar to the perspex thickness and larger, and as long as the flow structures do not change too quickly over time.

Considering that both, the liquid-crystal method [20] and the infrared method reflect the temperature field of the fluid near the surface through which the images are recorded, the design of our experiment was based on a relatively thin square enclosure as opposed to a cubic enclosure. This was chosen with the aim to observe a representation of the bulk flow rather than a boundary layer structure of an intrinsic 3-dimensional flow.

## 2. Theoretical formulation

Ferromagnetic fluids have usually a very small electric conductivity and electric effects are often neglected [6, 11]. In line with this, the fluid is assumed to be non-conductive and does not induce an electromagnetic current. Consequently, the magnetic field generated by the permanent magnet conforms to Maxwell's equations for non-conductive material in static form, represented as

$$\nabla \times \mathbf{H} = 0 \quad (1)$$

$$\nabla \cdot \mathbf{B} = 0 \quad (2)$$

where  $\mathbf{H}$  is the magnetic field and  $\mathbf{B}$  the magnetic induction. By definition the magnetic field and magnetic induction are related in the following manner

$$\mathbf{B} = \mu_0 (\mathbf{H} + \mathbf{M}) \quad (3)$$

where  $\mu_0 = 4\pi \times 10^{-7}$  H/m is the permeability of free space and  $\mathbf{M}$  the magnetisation of the magnetic material. Hence, the magnetisation of a permanent magnet may be written as  $\mathbf{M} = \mathbf{B}_r/\mu_0$  where  $\mathbf{B}_r$  is the remanent flux density of the magnet. The assumed magnetic field,  $\mathbf{H}$ , within the fluid domain is considered dependent on the initial Langevin susceptibility

$$\chi_L = \frac{nm^2}{3\mu_0 k_B T} \quad (4)$$

and modified after Pshenichnikov et al [32] to include inter-particle interactions and written as

$$\chi = \chi_L (1 + \chi_L/3) \quad (5)$$

where  $n$  is the particle number density and equals to  $(\mu_0 \phi M_d/m)$ ,  $m$  the magnetic moment of the ferromagnetic nanoparticles,  $k_B$  the Boltzmann's constant and  $T$  the temperature. Thus, the actual magnetic field acting on the magnetic fluid may be written as

$$\mathbf{H} = \frac{\mathbf{B}}{\mu_0 (1 + \chi)} \quad (6)$$

and conforms to Maxwell's equations, eq.(1) and eq.(2), in static form.

The strength of the magnetisation,  $M$ , for a monodispersed colloidal magnetic fluid is expressed as a function of the magnetic field intensity, the temperature and the concentration of dispersed magnetic particles. By applying Langevin's function  $\mathcal{L}(\zeta) = \coth(\zeta) - 1/\zeta$  the

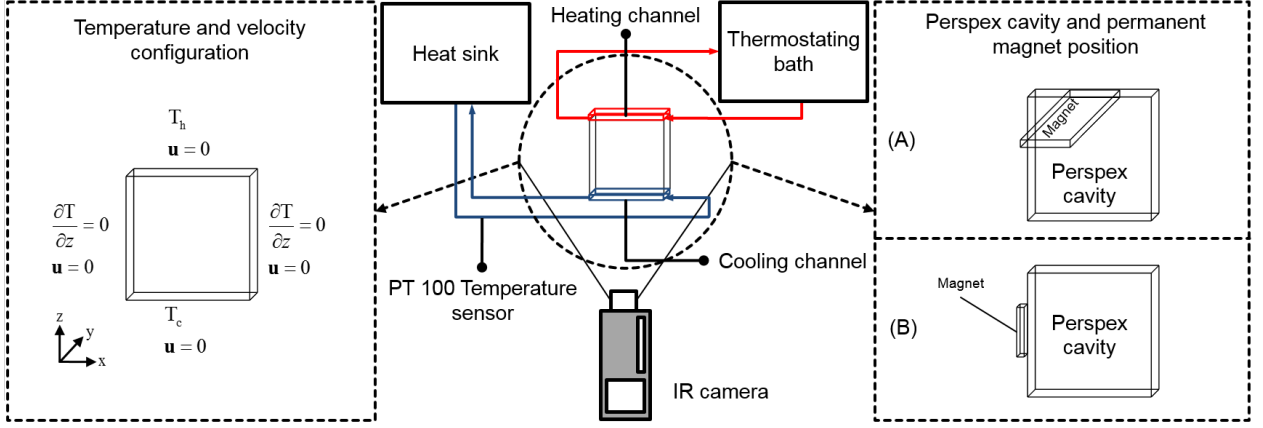


Figure 1: Schematic view of experimental apparatus, with temperature and velocity configurations on the left and permanent magnet configuration on the right.

equilibrium magnetisation of a ferromagnetic fluid may be written as

$$M_L(H, T, \phi) = \phi M_d \mathcal{L}(\zeta), \quad \zeta = \frac{mH}{k_B T} \quad (7)$$

where  $M_d$  is the bulk magnetic of the solid modified by the volume fraction  $\phi$  and  $H$  the magnitude of the magnetic field. However, inter-particle interactions within magnetic fluids are common and the argument in the Langevin function in eq.(7) may be extended in the same way as the susceptibility in eq.(5) to

$$\zeta_p = \frac{m(H + M_L/3)}{k_B T} \quad (8)$$

Furthermore, by assuming that the magnetic moment of the fluid is always aligned with the applied magnetic field,  $\mathbf{H}$ , [6, 32] Langevin's eq.(7) may be written as

$$\mathbf{M}_P = \frac{\mathbf{H}}{H} \phi M_d \mathcal{L}(\zeta_p) \quad (9)$$

The continuity and momentum equations for an incompressible magnetic fluid use the Boussinesq approximation and are represented as

$$\nabla \cdot \mathbf{u} = 0 \quad (10)$$

and

$$\rho_0 (\mathbf{u} \cdot \nabla) \mathbf{u} = -\nabla p + \mu \nabla^2 \mathbf{u} + \mathbf{f} \quad (11)$$

where  $\mathbf{u}$  is the velocity and  $p$  the pressure, respectively, while  $\rho_0$  is the density and  $\mu$  the dynamic viscosity at the reference temperature,  $T_0$ . The force term  $\mathbf{f}$  could represent either one or both of the two forces, buoyancy [33]

$$\mathbf{f}_b = \rho_0 \beta \Delta T \mathbf{g} \quad (12)$$

with  $\beta$  the volumetric expansion coefficient at  $T_0$ ,  $\Delta T = T - T_0$  and  $\mathbf{g}$  the gravitational acceleration, and the Kelvin body force

$$\mathbf{f}_K = \mu_0 (\mathbf{M}_P \cdot \nabla) \mathbf{H} + \frac{\mu_0}{2} \nabla \times (\mathbf{M}_P \times \mathbf{H}) \quad (13)$$

due to the influence of a magnetic field gradient. As fluid velocities are small in natural convection and with a stationary applied magnetic field, one can assume that the magnetic moment of the fluid is always aligned with the external magnetic field, eq.(9). Under these conditions, the fluid can be considered free from magneto-dissipation and the last term in eq.(13) may be neglected as was done in our study [5, 34, 35].

The heat equation, solving for temperature,  $T$ , is

$$\rho c_p (\mathbf{u} \cdot \nabla) T = k \nabla^2 T \quad (14)$$

where  $c_p$  is the specific heat capacity and  $k$  the thermal conductivity of the fluid.

### 3. Experimental setup

#### 3.1. Apparatus and system dimensions

The schematic of the experimental setup is presented in Fig. 1. The system consisted of a perspex cavity with the dimensions of 50 mm by 50 mm by 10 mm filled with a mineral oil based ferromagnetic fluid, a temperature controlled thermostat water bath, a heat sink, a PT100 temperature sensor, an infrared camera with data acquisition system and a permanent magnet with dimensions of 60 mm by 30 mm by 3 mm having a remanent flux density of  $B_r = 1$  Tesla with its poles at the large 60 mm by 30 mm surfaces. The cavity was subjected to thermal forcing by maintaining two opposite boundaries at different temperatures by pumping water from a thermostating water bath through a heating channel, and from a heat sink through the cooling channel in the cavity walls. The heat sink was monitored by a PT100 temperature sensor to keep the temperature constant at  $T_c = 20^\circ\text{C}$ . All four remaining walls were insulated. The permanent magnet was used in two configurations to provide an external magnetic field by placing the magnet with a distance of 5 mm either above the centre of the top heated wall for case (A) or to the left of the centre left adiabatic wall for case (B), both shown in the right hand side of Fig. 1.

magnetic particles		carrier liquid		magnetic fluid	
Property	Value	Property	Value	Property	Value
$\rho_s$	5175 kg/m <sup>3</sup>	$\rho_f$	838 kg/m <sup>3</sup>	$\rho$	1272 kg/m <sup>3</sup>
$k_s$	0.29 W/(m·K)	$k_f$	0.1107 W/(K·m)	$k$	0.129 W/(m·K)
$c_{p,s}$	151 J/(kg·K)	$c_{p,f}$	1710 J/(kg·K)	$c_p$	1554 J/(kg·K)
$\beta_s$	$0.13 \times 10^{-4} \text{ K}^{-1}$	$\beta_f$	$6.4 \times 10^{-4} \text{ K}^{-1}$	$\beta$	$3.85 \times 10^{-4} \text{ K}^{-1}$
$m$	$2.93 \times 10^{-25} \text{ J}\cdot\text{m}/\text{A}$	$\mu_f$	$2.0912 \times 10^{-2} \text{ Pa}\cdot\text{s}$	$\mu$	$2.614 \times 10^{-2} \text{ Pa}\cdot\text{s}$
$M_d$	4.23 kA/m	$\nu_f$	$2.495 \times 10^{-5} \text{ m}^2/\text{s}$	$\nu$	$2.055 \times 10^{-5} \text{ m}^2/\text{s}$
$\phi$	0.1	$\text{Pr}_f$	323	$\text{Pr}$	316

Table 1: Fluid properties, estimated for the experimental fluid and used for the simulations.

### 3.2. Fluid properties

The working fluid was a commercially available magnetic fluid with dispersed magnetite particles in a mineral oil based carrier fluid. As only limited information was available, the physical properties of the fluid had to be estimated. Our numerical study estimated the properties of those from the magnetic particles and the carrier fluid and are summarised in Table 1 where the subscript (*s*) denotes the values for the solid dispersed magnetite particle and (*f*) for the carrier fluid, respectively. Using the volume fraction,  $\phi$ , the magnetic liquid properties can be estimated as the density:

$$\rho = \phi \rho_s + (1 - \phi) \rho_f \quad (15)$$

the thermal conductivity:

$$k = \phi k_s + (1 - \phi) k_f \quad (16)$$

the heat capacity:

$$c_p = \phi c_{p,s} + (1 - \phi) c_{p,f} \quad (17)$$

the thermal expansion coefficient [36]:

$$\beta = \frac{\phi \rho_s}{\rho} \beta_s + \frac{(1 - \phi) \rho_f}{\rho} \beta_f \quad (18)$$

and the dynamic viscosity [37]:

$$\mu = \mu_f \left( 1 + \frac{5}{2} \phi \right) \quad (19)$$

### 3.3. Measurements and image processing

The infrared camera used was a FLIR T620bx [38] having a spectral range of 7.5-14  $\mu\text{m}$  and is applicable for a thermal range of -40 to +150  $^\circ\text{C}$  with a sensitivity of 30 mK @ +30  $^\circ\text{C}$ . The IR image resolution is 640×480 pixels. This camera was placed with a distance of 0.4 m from the experimental system to measure the surface temperature of the experimental system. The thermostating bath and heat sink temperature were monitored and adjusted to provide a constant temperature throughout the measurement period. The live view of the infrared camera could be used to observe the evolving temperature field and determine if the flow had clearly settled into a stable final state after around 15 minutes. After the settling period, the surface temperature was recorded by an infrared image frame with a temperature scale superimposed by the camera.

While the infrared camera captures the temperature of the outside of the perspex wall, this reflects the fluid temperature through conduction of heat through the perspex wall as long as the size of fluid temperature features is similar to the wall thickness or larger. The fluid temperature was therefore estimated by using the surface infrared images calibrated against the in-situ temperature measurements from the thermocouple probes in the heating and cooling channels. As the signal from those measurements has to go through the same perspex walls, and the two temperatures measured directly are the minimum and maximum occurring in the system, they provide two reliable calibration points to calibrate the temperature measurements from the infrared images to reconstructed fluid temperatures. The measurement points were set manually by using the cameras software to coincide with the thermocouples. Thus, the recorded IR image frames that uses the infrared temperature scale added by the camera were extracted from the system and post-processed to transfer the RGB values into a temperature matrix. The temperature scale of this matrix was then adjusted to the temperature scale that was measured by the temperature sensors. This technique provided an adequate correction of the radiation detected by the radiometer and included the emissivity corrections.

To compare experimental with numerical results, the temperature matrix was non-dimensionalised and plotted with a temperature color bar scaled to match the CFD settings. Both experimental and numerical non-dimensional temperature profiles are shown in Fig. 3 for case (A) and Fig. 5 for case (B). The experimental and numerical results and their discussion are given in §5 and §6, respectively.

### 3.4. Non-dimensional Parameters

In this section, the main non-dimensional parameters to characterise heat transfer by natural and thermomagnetic convection are introduced. A quantitative non-dimensional parameter to characterise the strength of the driving force in natural convection is the Rayleigh number, Ra, and is found as the balance of buoyancy to viscous dissipation and heat diffusion,

$$\text{Ra} = \frac{\beta \Delta T g L^3}{\nu \kappa} \quad (20)$$

where  $L$  is the characteristic length scale of the system,  $\Delta T$  the temperature difference imposed across the sys-

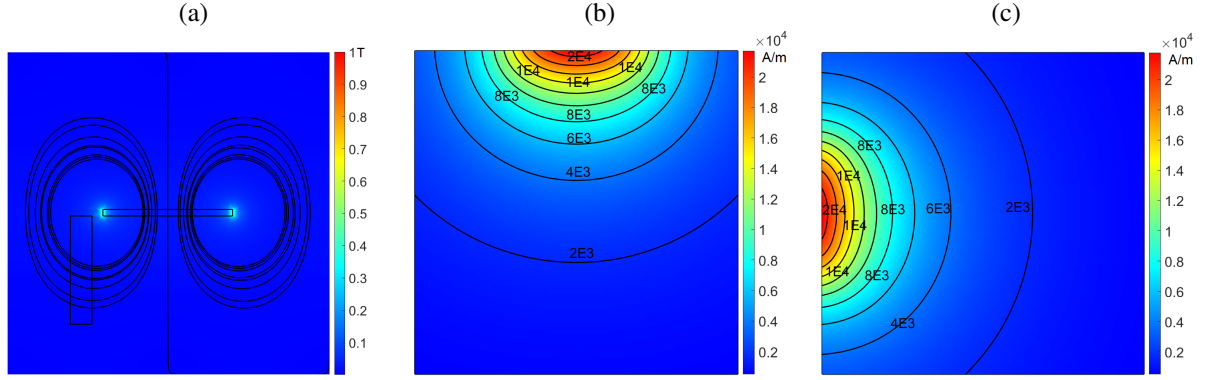


Figure 2: (a) Field lines and induction field,  $\mathbf{B}$ , in the  $y$ - $z$  plane for configuration (A). Contour plot of the magnetic field strength,  $H$  in the  $x$ - $z$  plane inside the convection cell for configuration (A) in (b) and configuration (B) in (c), respectively.

tem,  $\nu$  the kinematic viscosity and the thermal diffusivity  $\kappa = k/(\rho c_p)$ . Following eq.(5), eq.(9) and eq.(13) a similar process is found in thermomagnetic convection. Without a temperature gradient the fluid remains stable according to adiabatic compression and magnetisation. However, in the presence of a temperature gradient, the magnetisation of the fluid will additionally change with respect to the pyromagnetic coefficient,  $K$ ,

$$K = - \left( \frac{\partial M_p}{\partial T} \right)_{\phi, H} \quad (21)$$

which includes inter-particle interactions. Thus, non-isothermal perturbations of the magnetisation always leads to convective instability [5]. A force balance of magnetic to viscous dissipation may be expressed as a magnetic Rayleigh number,  $Ra_m$ , and written as

$$Ra_m = \frac{\mu_0 K \Delta T H L^2}{\rho \nu \kappa} \quad (22)$$

The governing equations can be non-dimensionalised using suitably chosen reference scales. For natural and thermomagnetic convection, the most appropriate velocity scale is the viscous velocity scale given by the characteristic length of the system,  $L$ , and the kinematic viscosity,  $\nu$ , as  $\nu/L$ . Using this and the following non-dimensional variables

$$\begin{aligned} u' &= \frac{uL}{\nu}, & \nabla' &= \nabla L, & p' &= \frac{pL^2}{\rho \nu^2} \\ T' &= \frac{T - T_c}{T_h - T_c}, & M' &= \frac{M_p}{M_s}, & H' &= \frac{\mu_0 H}{B} \end{aligned} \quad (23)$$

equations (10)-(14) may be expressed in non-dimensional form as

$$\nabla' \cdot \mathbf{u}' = 0 \quad (24)$$

$$\begin{aligned} (\mathbf{u}' \cdot \nabla') \mathbf{u}' &= -\nabla' p' + \nabla'^2 \mathbf{u}' \\ &+ \frac{T'}{\text{Pr}} \left[ Ra \mathbf{e}_g + Ra_m (\mathbf{M}' \cdot \nabla') \mathbf{H}' \right] \end{aligned} \quad (25)$$

$$(\mathbf{u}' \cdot \nabla') T' = \text{Pr} \nabla'^2 T' \quad (26)$$

where  $\mathbf{e}_g$  is the unit vector in direction of gravity, and  $\text{Pr}$  is the Prandtl number,

$$\text{Pr} = \frac{\nu}{\kappa}. \quad (27)$$

An overall force balance to characterise thermomagnetic convection contains therefore two additive terms, buoyancy and thermomagnetic, which can be used to define an appropriate non-dimensional parameter. To provide a framework for a quantitative comparison, a modified Rayleigh number,  $Ra^*$ , is defined by taking the relative orientation into account. For the first configuration where the dominant field gradient in the vertical is in the opposite direction to gravity, the  $Ra^*$  is calculated as the net difference of the thermogravitational and thermomagnetic part in the following manner

$$Ra^* = \left( \frac{\mu_0 |K| H}{L} - \rho \beta g \right) \frac{L^3 \Delta T}{\rho \nu \kappa} \quad (28)$$

For the second simulation, where the main magnetic field gradient is horizontal and therefore perpendicular to gravity, the overall net effect can be estimated as the vector sum,

$$Ra^* = \sqrt{Ra^2 + Ra_m^2} \quad (29)$$

The resulting heat transfer across the heated cavity of length,  $L$ , can be quantified by the dimensionless Nusselt number,  $Nu$ , which is the ratio of the total heat transfer,  $Q$ , to the conductive heat transfer,  $Q_0 = kA\Delta T/L$ , across a surface,  $A$ . Therefore, the Nusselt number can be determined by

$$Nu = \frac{L}{k \Delta T} \frac{1}{A} \int q dA \quad (30)$$

by integrating the total heat flux across a cross-section,  $A$ , where  $Nu = 1$  would indicate a heat transfer by conduction alone and  $Nu > 1$  an enhanced heat transfer by convection.

## 4. Numerical model

### 4.1. Numerical model set-up

The numerical model was configured to the same physical specifications as the experiment and is represented with its temperature and boundary conditions in

the left panel of Fig. 1. The cavity is cooled at the bottom wall with  $T_c = 290$  K, heated at the top wall with  $T_h = T_c + \Delta T$  and thermally insulated at all remaining walls. Boundary conditions for velocity are no-slip at all side walls. At the top left corner of the cavity, a zero pressure constraint was applied. All configurations used were started with the same initial conditions of a uniform distributed temperature of  $T_c$ , a stagnant fluid and an initial zero gauge pressure.

#### 4.2. Numerical methodology

The magnetic field, heat and fluid flow equations were solved numerically with the use of the Finite-Element solver developed by COMSOL Multiphysics [39]. A tetrahedral mesh was generated with 4,011,242 elements where most of the elements (3,437,223) were allocated in the fluid domain. Convergence tests at lower resolution suggested that the model converged to the final solution reliably for a mesh with at least 3 million elements. All solutions were produced by using a parametric non-linear solver for stationary solutions that allowed to sweep a given parameter, e.g. the temperature boundary conditions.

To ensure that the magnetic field within the fluid domain was correctly calculated, the magnetic field was solved in an extended domain of a cube with edge length  $3L$ . At the boundary of the extended domain, zero magnetic scalar potential was applied. The permanent magnet was placed in the center of the extended domain having a remanent flux density of  $\mathbf{B}_r = (0, 0, B_r)$  for configuration (A) or  $\mathbf{B}_r = (B_r, 0, 0)$  by using configuration (B). The fluid domain was placed according to study cases (A) and (B) within the extended domain. A linear solver was used to calculate the static magnetic field, eq.(1), eq.(2) and eq.(3) in the full domain. Results of the computed induction field  $\mathbf{B}$  are presented with field lines in Fig. 2(a). From this step, only the solution for  $\mathbf{B}$  was used in the following process of solving the heat and fluid flow equations to calculate the magnetic field,  $\mathbf{H}$ , within the fluid domain using eq.(6). Results of the magnetic field,  $\mathbf{H}$ , are presented for configuration (A) and (B) in Fig. 2(b) and (c) respectively.

The calculated magnetic field,  $\mathbf{H}$ , and the temperature of the fluid then provided the magnetisation,  $\mathbf{M}_p$ , for calculating the Kelvin body force using eq.(13). Thus, the continuity, eq.(10), momentum, eq.(11), and heat, eq.(14) are solved simultaneously using this Kelvin force and buoyancy as the body forces.

### 5. Results

Here we present first the experimentally observed temperature fields together with the corresponding temperature and velocity fields from the numerical model in §5.1 for configuration (A) and §5.2 for configuration (B), followed by an analysis of the resulting heat transfer in §5.3. A comparison of the experimental and numerical simulations is addressed in §6.

#### 5.1. Thermomagnetic convection with magnet at top

Without the magnets, the temperature conditions imposed shown in Fig. 1 would result in a stagnant, stably stratified fluid with equally-spaced horizontal isothermal contour lines; all heat transfer occurs through conduction alone. However, in presence of the permanent magnet placed at configuration (A), the Kelvin body force creates a thermomagnetically induced convection distorting the isotherms. The experimental temperature fields from the infrared thermography for case (A) are presented for two temperature differences in Fig. 3 alongside the computed temperature and velocity fields from the corresponding model simulations. All temperature plots present a temperature distribution that is indicative of enhanced heat transfer due to a weak flow of magnetic fluid which moves upwards against gravity in the center of the fluid domain towards the position of the magnet shown in Fig 3(e) and (f). The observed flow can be interpreted that cooler and therefore more strongly magnetised fluid flows towards higher magnetic field regions and forces less magnetised warmer fluid away.

By increasing the temperature difference seen in the second row of Fig. 3 the convective flow increases in the top of the fluid domain whereas the bottom appears to be little affected. The difference of the convection at different temperatures can be identified by vertical temperature profiles through the centre of the fluid domain, shown in Fig. 4 where each curve corresponds to panels (a) to (d) of Fig. 3, respectively. All four curves show a similar linear temperature rise from the bottom of the fluid to a point at around 30 to 40% of the depth where the nonlinear temperature gradient in both simulations is  $dT'/dz' = 1.761 \pm 0.003$ . In the experiments, the gradient is a little less; at  $\Delta T = 10$  K:  $dT'/dz' = 1.44 \pm 0.01$  and at  $\Delta T = 20$  K:  $dT'/dz' = 1.55 \pm 0.01$ .

Above the linear region, the numerical simulations show a gradual decrease of the temperature gradient, reaching an isothermal region between  $z' \approx 0.75$  and  $0.98$ , indicating convective heat transfer. Above this mixed region, a thermal boundary layer is seen with a temperature gradient at the wall of  $dT'/dz' = 7.69$  at  $\Delta T = 10$  K and  $dT'/dz' = 7.95$  at  $\Delta T = 20$  K, respectively. The thermography results for  $\Delta T = 20$  K follow the computational results closely over a substantial range but do not resolve the boundary layer. The results for  $\Delta T = 10$  K remain below the computed results in the convective region but even then, there is a distinct reduction in the temperature gradient, confirming the presence of convective heat transfer. The transition between the stagnant conduction layer at the convective region occurs in the experiments at around  $z' = 0.43$  and  $0.5$ , for  $\Delta T = 10$  K and  $20$  K respectively, while it occurs at  $z' = 0.29$  and  $0.32$  in the simulations.

#### 5.2. Thermomagnetic convection with magnet at side

When the permanent magnet is placed at the second configuration (B), left of the perspex cavity to create a horizontal magnetic field gradient, a similar effect of

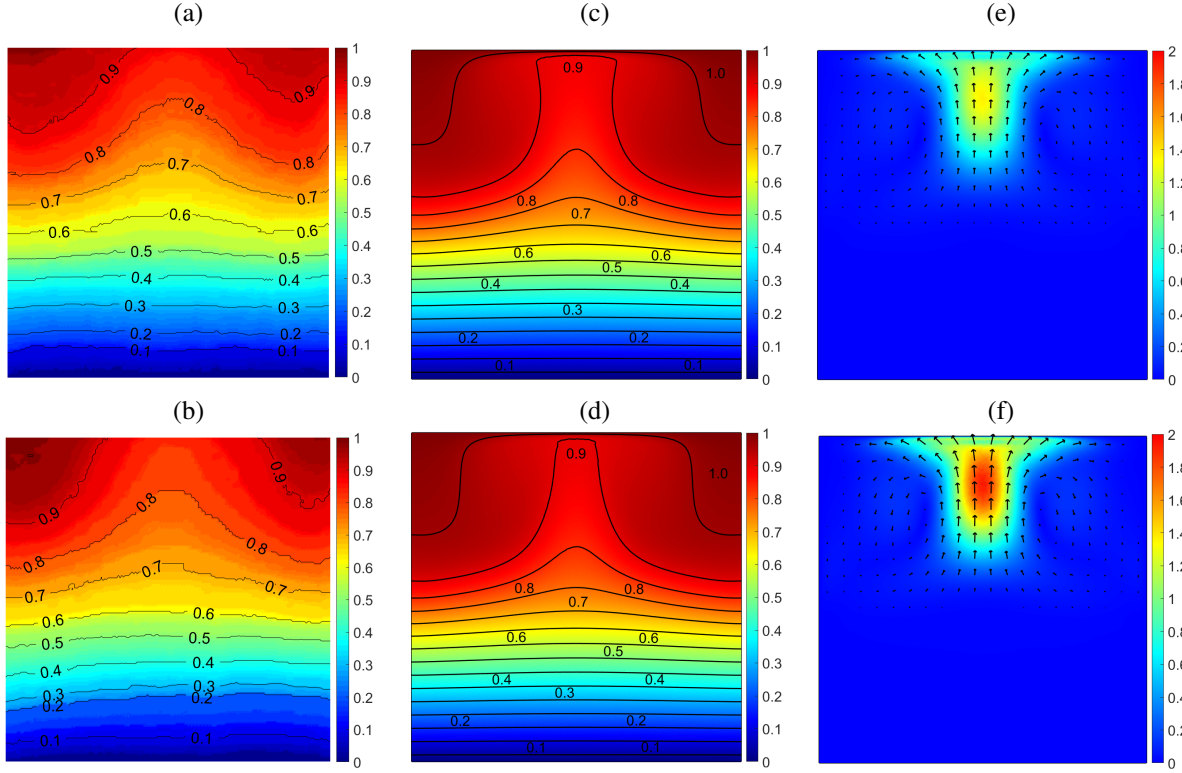


Figure 3: Non-dimensional experimental temperature fields in (a), (b) , non-dimensional computed temperature (c), (d) and velocity fields (e), (f) for  $\Delta T = 10$  K,  $Ra^* = 1.93 \times 10^7$  in the top row and  $\Delta T = 20$  K,  $Ra^* = 3.71 \times 10^7$  in the bottom row using magnetic configuration (A).

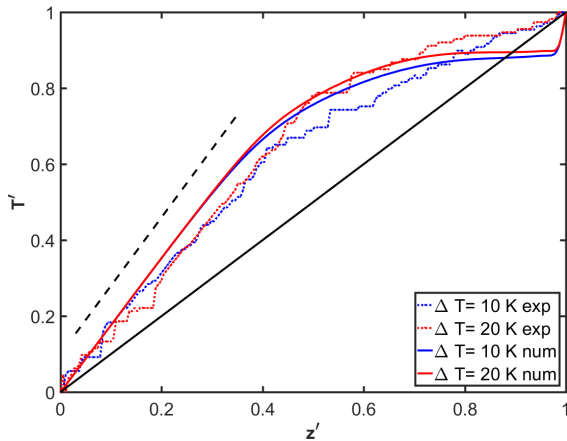


Figure 4: Non-dimensional experimental and simulated temperature profiles for the vertical cross-section through the centre of the tank using magnetic configuration (A). The solid black diagonal is the conduction-only solution and the dashed black line indicates the non-dimensional temperature gradient of  $dT'/dz' = 1.8$ .

magnetically induced convection is observed. Experimental and numerical results are shown in Fig. 5 this time with the isotherms pulled up at the left side of the cavity, nearest the magnet. As the resulting Kelvin body force is now perpendicular to buoyancy a weak convective flow of cooler magnetic fluid from the bottom cooled wall towards the magnet is observed and presented in Fig. 5. The accelerated fluid from the bottom then moves upwards against gravity towards the magnet and forms a convective cell. Since the Kelvin body force becomes weaker further away from the magnet the stable stratification of the fluid under gravity becomes visible in the right part of the fluid domain where the fluid moves very slowly, as shown in Fig. 5(e). By increasing the temperature difference it is observed in Fig. 5(f) that the convective flow increases overall. This suggests an increase of heat transfer through the complete system.

Figure 6 shows vertical temperature profiles for the experiments and numerical results with the magnet at the side in Fig. 6(a) and horizontal profiles in Fig. 6(b). The vertical profiles again show good correspondence between observations and simulations. Compared to configuration (A) with the magnet on top, the profile is much closer to the diagonal which represents heat transfer by conduction only. The region with the lowest vertical temperature gradient, which indicates mixing of heat by convection, is found in a region between  $0.2L$  from the bottom and mid-height above which the temperature profile becomes gradually more linear, reaching a constant temperature gradient of, at  $\Delta T = 10$  K:

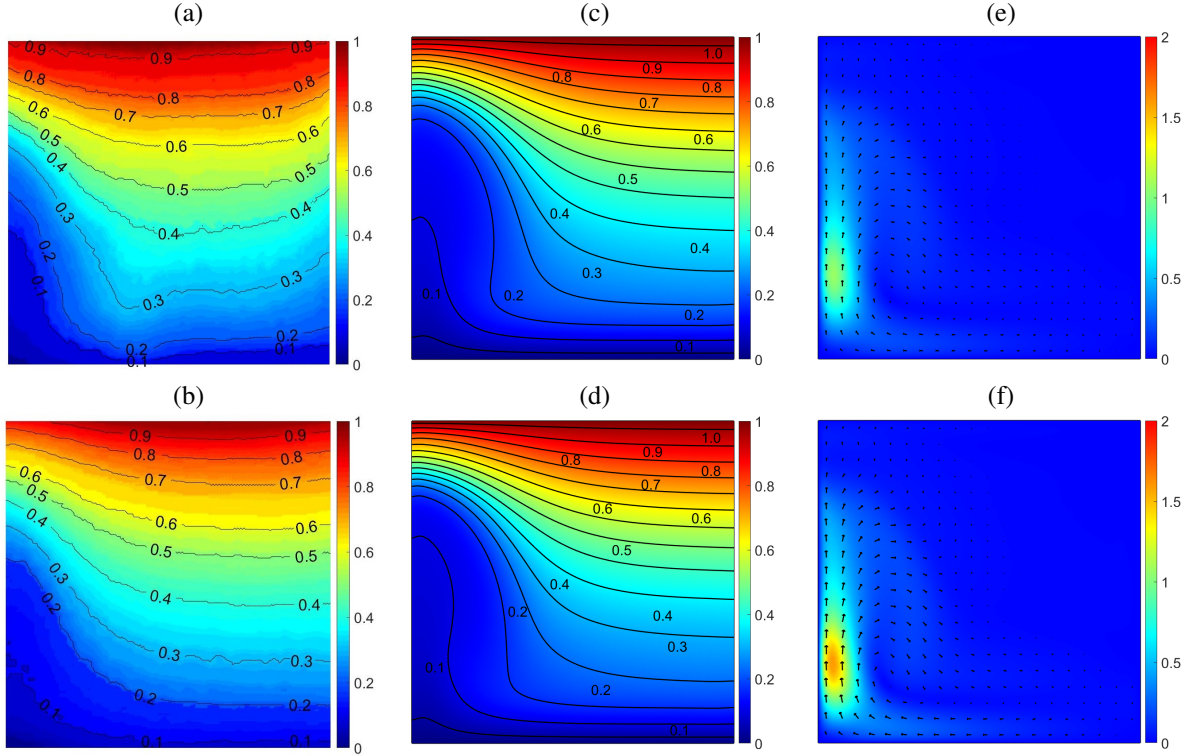


Figure 5: Non-dimensional experimental temperature fields in (a), (b) , non-dimensional computed temperature (c), (d) and velocity fields (e), (f) for  $\Delta T = 10$  K,  $Ra^* = 4.33 \times 10^6$  in the top row and  $\Delta T = 20$  K,  $Ra^* = 8.22 \times 10^6$  in the bottom row using magnetic configuration (B).

$dT'/dz' = 1.30$ , and at  $\Delta T = 20$  K:  $dT'/dz' = 1.37$  and very little convective heating in the upper 20% of the domain. This is confirmed by the velocity arrows in Fig. 5(e) and (f). The convective region extends further down at the higher temperature difference.

The horizontal temperature gradient, taken at mid-height for Fig. 6(b), shows very low temperatures within about  $0.1L$  of the left boundary, followed by a rapid temperature increase to a fairly constant level at around  $0.4L$ . While the temperature profiles are generally well aligned between experiments and simulations, the experiments did not show the general decrease of the profile seen in the simulations in the step from  $\Delta T = 10$  K to 20 K. In the simulations, the temperature profile at  $\Delta T = 20$  K compared to that at  $\Delta T = 10$  K showing that the convective cooling near the magnet is more intense resulting in an overall reduction of the temperature across the domain. While the simulations reach the highest temperature at the insulated wall on the right side, the thermography measures temperature maxima within the fluid interior followed by a drop towards the right wall, especially at the lower temperature difference.

### 5.3. Heat transfer by thermomagnetic convection

The heat transfer across the cavity is investigated using the CFD model and quantified by the dimensionless Nusselt number that is plotted versus a set of twelve temperature differences in Fig. 7 and the modified Rayleigh number in Fig. 8. As presented in Fig. 7, both magnetic configurations increase heat transfer via

thermomagnetic convection compared to the conduction case. However, the increase in heat transfer differs between the magnetic configurations. When the magnet is placed at configuration (A), the Nusselt number peaks at 1.63 and then decreases slowly. This is not the case for configuration (B) where the Nusselt number continues to increase with increasing temperature differences approaching the value  $Nu=1.9$ . Figure 8 reflects both results where the same peak in Nusselt number for configuration (A) occurs at  $Ra^* = 3.71 \times 10^7$  after which the Nusselt number decreases when the modified Rayleigh number is increased further.

## 6. Discussion

In this section, a critical comparison of the thermography observations with the corresponding numerical results attempts to identify the robust features of thermomagnetic convection observed in the experiments and then to identify the underlying process leading to the observations.

Reviewing the main differences between the numerical and experimental results highlights as the most dominant features the rising isotherms at the sides and the less sharp temperature gradients near the magnets in the thermography images compared to the model results. While the numerical model has perfectly insulated side walls with resulting horizontal isotherms, the side walls of the apparatus are imperfectly insulated leading to heat loss through the sides, especially from the warmer fluid. The reduced temperature gradients near

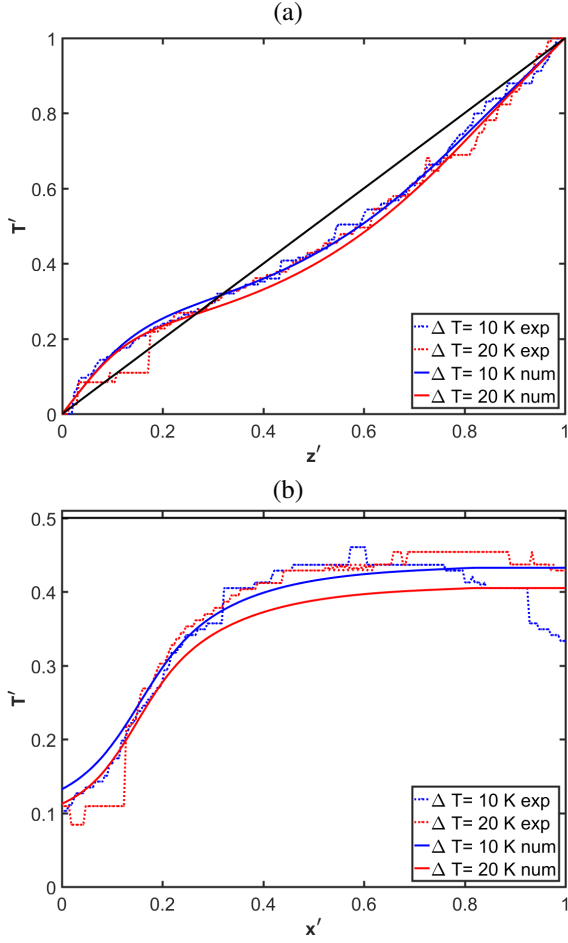


Figure 6: Non-dimensional experimental and simulated temperature profiles for the vertical cross-section in (a) and horizontal in (b) through the centre of the tank using magnetic configuration (B).

the magnets could be a result of the magnet itself or the imaging technique. The numerical model assumes a permanent magnet with sharp edges and uniform remanent flux across the pole surfaces. Slight imperfections in the

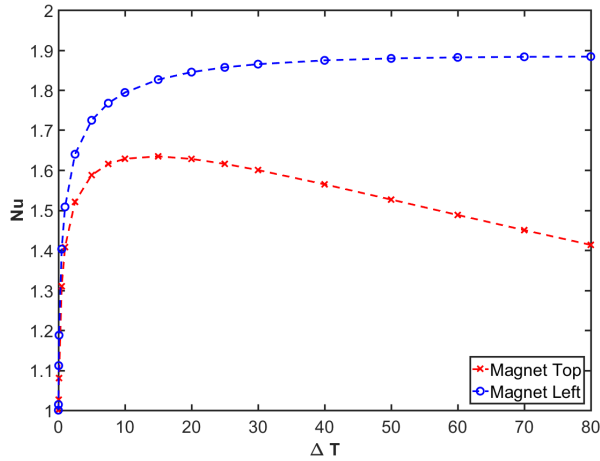


Figure 7: The Nusselt number,  $Nu$ , versus the temperature difference,  $\Delta T$ .

magnet, such as slightly rounded edges or non-uniform surface magnetisation, could lead to reduced magnetic field gradients especially near the edges. Furthermore, the imaging techniques of thermography 'through' the perspex wall leads to a spatial resolution of the infrared images on the order of the thickness of the perspex sheet of a few millimetres. Considering that the thermal boundary layer observed in Fig. 4 has a thickness of 2% of the fluid depth, or 1 mm, such features cannot be expected to be resolved adequately.

In the light of this, the simulations in panels (c) and (d) of Fig. 3 show a remarkable qualitative and quantitative agreement with their corresponding experimental observations in panels (a) and (b), in particular in location where the horizontal isotherms change to the isotherms shifted upwards in the centre of the tank underneath the magnet, and in the spacing of the isotherms. Not only do the simulated temperature fields closely mimic the observations, but also the subtle shift in the location of the transition from the conductive lower layer to the convective upper layer towards a higher position at the higher temperature is captured by experiments as well as simulations, as shown in Fig. 4. Furthermore, our results for configuration (A) show good agreement with the numerical simulations by Chang et al [17]. Taking this agreement as validation of the numerical model, the velocity fields in Fig. 3(e) and (f) can be used to interpret the observed temperature field indeed as the result of thermomagnetic convection. As suggested by the governing equations, the magnetic field gradient causes through the Kelvin body force a stronger attraction of the cooler fluid below the warmer fluid towards the magnet. This is then complemented with warmer fluid flowing in two convection cells outwards and downwards to the side of the central region. The extent of the convection cells shown in the flow fields suggests that the influence of the Kelvin body force becomes insufficient to overcome buoyancy, resulting in the organisation of the flow into the gravitationally stable lower layer and the thermomagnetically

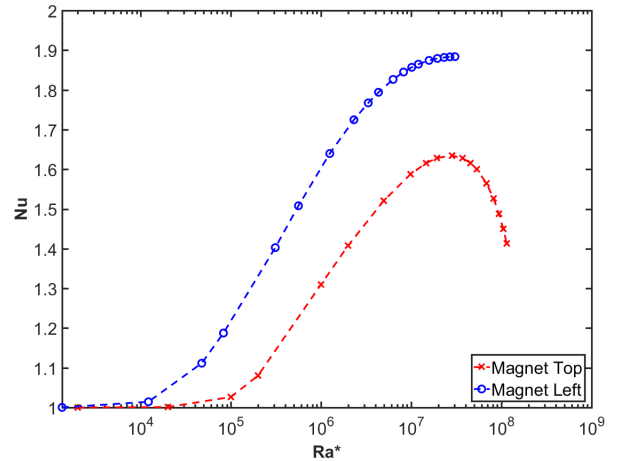


Figure 8: The Nusselt number,  $Nu$ , versus the modified Rayleigh number,  $Ra^*$ .

forced upper layer.

All these arguments can be directly translated to the other configuration, (B), where the Kelvin body force is now strong enough to induce thermomagnetic convection in a single convection cell with a maximum response in the part of the fluid domain which is coldest and closest to the magnet. There, the higher magnetisation of the fluid results in a very strong flow of the cold fluid towards the magnet. This then results in the organisation of the fluid into a strong convection cell in the region near the magnet, a stagnant region further away, and two weakly convective regions near the upper and lower boundaries. This weak convection can be explained that, while the stratification of the fluid due to gravity inhibits vertical motion, it does not impede horizontal motion. This horizontal motion is required to satisfy continuity in response to the thermomagnetic convection extracting fluid from the coldest region at the bottom surface and injecting fluid into the top region.

As the structure of the flow and temperature fields have been explained on the basis of the Kelvin body force inducing convection in part of the fluid and gravity inhibiting convection in the other, it is useful to quantify the relative strength of the Kelvin body force to buoyancy within the cavity. A measure of their force balance may be defined by

$$r = \log_{10} \left( \frac{Ra_m}{Ra} \right) \quad (31)$$

and is presented in Fig. 9 and Fig. 10 for magnetic configuration (A) and (B), respectively. The local  $Ra$  and  $Ra_m$  are calculated with eq.(20) and eq.(22) respectively by using the local values of the computed numerical solution of eq.(11)-(14). A value greater than zero indicates that the Kelvin body force is dominant at that point within the cavity whereas buoyancy dominates for a value less than zero. For  $r$  equal to zero, both forces are equal and presented as a black contour line.

Figure 9(a) presents the force ratio for a temperature difference of 10 K where the Kelvin body force dominates the top and buoyancy the bottom of the fluid domain. The observed clear maximum in the Nusselt number presented in Fig. 7 and Fig. 8 corresponds to the effective ratio of the body forces creating conductive heat transfer in the bottom and thermomagnetic convection in the top of the fluid domain.

A further increase in temperature difference above  $\Delta T = 10$  K indicates a decrease in heat transfer as both body forces increase but at a different rate, where the Kelvin body force increases more slowly because

$\Delta T$	(A)	(B)
10 K	0.2564	0.2627
20 K	0.2483	0.2614
80 K	0.2049	0.2548

Table 2: Nondimensional distance of the  $r = 0$  point along the centreline or mid-height from the wall adjacent to the magnet for configurations (A) and (B), respectively.

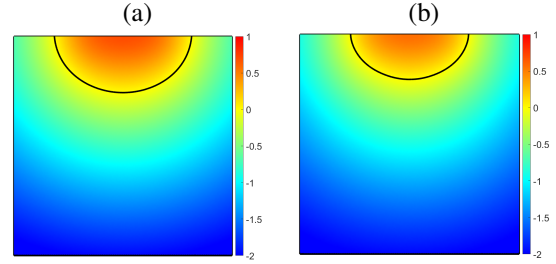


Figure 9: The relative influence of Kelvin body force on buoyancy,  $r$ , and their effect on convective fluid flow within the fluid domain at a temperature difference of (a)  $\Delta T = 10$ K,  $Ra^* = 1.93 \times 10^7$ , and (b)  $\Delta T = 80$ K,  $Ra^* = 1.15 \times 10^8$  for magnetic configuration (A).

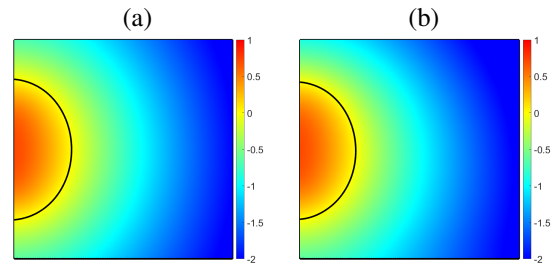


Figure 10: The relative influence of Kelvin force on buoyancy and their effect on convective fluid flow,  $r$ , within the fluid domain at a temperature difference of (a)  $\Delta T = 10$ K,  $Ra^* = 4.33 \times 10^6$ , and (b)  $\Delta T = 80$ K,  $Ra^* = 3.06 \times 10^7$  for magnetic configuration (B).

the pyromagnetic coefficient reduces, and the fluid domain becomes more buoyancy-dominated. The increase of a more buoyancy-dominated fluid domain is also observed in the corresponding temperature profile in Fig. 3 (a) where the 0.6 isothermal contour line becomes more horizontal at a temperature difference of  $\Delta T = 20$  K in (b) indicating heat transfer by conduction in this part of the fluid where convection is seen at the lower temperature difference. In particular, the pyromagnetic coefficient,  $K$ , varies only weakly with temperature in a very strong magnetic field where the fluid's magnetisation has reached saturation but decreases strongly with increasing temperature in a weak magnetic field. The result is therefore that  $r$  is not much affected very close to the magnet but reduces rapidly a little further away from the magnet, shifting in particular the line where buoyancy and Kelvin body force have equal magnitude closer to the magnet. The same is observed for configuration (B) where the magnet is to the left of the fluid. This trend is continued as the temperature increases further beyond the range explored in the experiment. Table 2 summarises the effect of the temperature dependence of the pyromagnetic coefficient on the force balance by showing the distance from the wall along the centreline where buoyancy and Kelvin body force have equal magnitude, i.e.,  $r = 0$ , for the experimental conditions described earlier as well as a temperature difference of  $\Delta T = 80$  K. Here, the shift of that location is only around 3.2% between 10 K and 20 K, consistent with the subtle shifts observed in Figures 4 and 6, but

20% difference between 10 K and 80 K for configuration (A) and around 3% for configuration (B). The difference in this temperature effect can be understood by the fact the main direction of the magnetic field gradient is aligned with the temperature gradient in configuration (A). In contrast, the horizontal section for configuration (B) encounters a much smaller temperature gradient further away from the magnet which reduces the impact on the pyromagnetic coefficient. This then results in intensified convection closer to the magnet as the thermal forcing is increased but also a reduction of the thermomagnetic forcing further away leading to a counteracting balance of enhancing the total heat transfer as the Rayleigh number is increased against a reduction in the magnetic effect on the heat transfer as the region of influence of the magnetic forcing become smaller. The decrease in the Nusselt number observed after a clear maximum in Fig. 8 reflects the shift from the effect of intensifying the strength of convective flow near the magnet to reducing the spatial extent of that convective flow.

## 7. Conclusion

This study has analysed thermomagnetic convection experimentally by infrared thermography and numerically by a finite-element model that provided corresponding temperature and flow fields. The parametric numerical study explained the dependence of temperature on the Kelvin body force to correlate the resulting heat flux and temperature profile within the cavity according to the experimental results. Both experimental and numerical models showed good agreement. A non-dimensional magnetic Rayleigh number was developed to characterise thermomagnetic convection and represents the empirical equivalent to the conventional Rayleigh number. The resulting heat transfer was quantified by the Nusselt number and evaluated against a modified Rayleigh number that accounted for both, buoyant and thermomagnetic effects.

In summary, we observed that an increase in temperature difference leads to an increase in both body forces. However, the intensity differs between the forces and can be calculated via a convective force ratio,  $r$ , of magnetic Rayleigh number and convectional Rayleigh number. Secondly, the Kelvin body force is stronger than buoyancy and can induce convection where buoyancy is not able to.

## Acknowledgements

This work was supported by the Konrad-Adenauer Foundation with a stipend to Peter Szabo.

## References

[1] S. Choi, J. Eastman, Enhancing thermal conductivity of fluids with nanoparticles, Technical Report, Energy Technology Division and Material Science Division Argonne National Laboratory Argonne, Illinois, 1995.

[2] L. Vékás, D. Bica, M. V. Avdeev, Magnetic nanoparticles and concentrated magnetic nanofluids: Synthesis, properties and some applications, *China Particuology* 5 (2007) 43–49.

[3] S. Odenbach, *Ferrofluids: Magnetically controllable fluids and their applications*, Springer, 2010.

[4] R. E. Rosensweig, *Ferrohydrodynamics*, Dover Publications, Dover, 1997.

[5] E. Blums, A. Cebers, M. M. Maiorov, *Magnetic fluids*, Walter de Gruyter & Co., 1996.

[6] R. Ganguly, S. Sen, I. K. Puri, Thermomagnetic convection in a square enclosure using a line dipole, *Physics of Fluids* 16 (2004) 2228–2236.

[7] A. Lange, S. Odenbach, Thermomagnetic convection in magnetic fluids subjected to spatially modulated magnetic fields, *Physics Procedia* 9 (2010) 171–175.

[8] M. Heckert, L. Sprenger, A. Lange, S. Odenbach, Experimental determination of the critical Rayleigh number for thermomagnetic convection with focus on fluid composition, *Journal of Magnetism and Magnetic Materials* 381 (2015) 337–343.

[9] R. A. Curtis, Flows and wave propagation in ferrofluids, *Physics of Fluids* 14 (1971) 2096–2102.

[10] D. P. Lalas, S. Carmi, Thermoconvective stability of ferrofluids, *Physics of Fluids* 14 (1971) 436–438.

[11] A. Mukhopadhyay, R. Ganguly, S. Sen, I. K. Puri, A scaling analysis to characterize thermomagnetic convection, *International Journal of Heat and Mass Transfer* 48 (2005) 3485–3492.

[12] S. Banerjee, A. Mukhopadhyay, S. sen, R. Ganguly, Effects of the dipole position on thermomagnetic convection in a locally heated shallow enclosure: Thermodynamic and transport analysis, *Numerical Heat Transfer, Part A* 57 (2010) 496–519.

[13] H. Aminfar, M. Mohammadpourfard, Y. N. Kahnamouei, Numerical study of magnetic field effects on the mixed convection of a magnetic nanofluid in a curved tube, *International Journal of Mechanical Sciences* 78 (2013) 81–90.

[14] D. Zablockis, V. Frishfelds, E. Blums, Numerical investigation of thermomagnetic convection in a heated cylinder under the magnetic field of a solenoid, *Journal of Physics* 20 (2008) 301–8.

[15] E. Blums, A. Mezulis, G. Kronkalns, Magnetoconvective heat transfer from a cylinder under the influence of a nonuniform magnetic field, *Journal of Physics* 20 (2008) 1–5.

[16] W.-G. Früh, Heat transfer enhancement by thermomagnetic convection, in: P. Jansens, A. Stankiewicz, A. Green (Eds.), *Sustainable (Bio)Chemical Process Technology*, BHR Group Ltd., Cranfield, 2005, pp. 47–56.

[17] C. M. Chang, W. T. Cheng, W. J. Liu, H. W. Cheng, C. E. Huang, S. W. Du, Thermal flow of fluid with magnetic particles in the presence of magnetic field, *International Communications in Heat and Mass Transfer* (2010).

[18] P. S. B. Szabo, W.-G. Früh, Enhanced and reduced natural convection using magnetic fluid in a square cavity, *Proceedings in Applied Mathematics and Mechanics* 16 (2016) 651–652.

[19] W.-G. Früh, Using magnetic fluids to simulate convection in a central force field in the laboratory, *Nonlinear Processes in Geophysics* 12 (2005) 877–889.

[20] T. Sawada, H. Kikura, T. Tanahashi, Visualization of wall temperature distribution caused by natural convection in a cubic enclosure, *International Journal of Applied Electromagnetics in Materials* 4 (1994) 329–335.

[21] S. M. Snyder, T. Cader, B. A. Finlayson, Finite element model of magnetoconvection of a ferrofluid, *Journal of Magnetism and Magnetic Materials* 262 (2003) 269–279.

[22] J. Mai, W.-G. Früh, Hot film measurements in a two-layer system of a magnetic liquid and a silicone oil, *Measurement and Science Technology* 15 (2004) 170–184.

[23] M. Reindl, A. Leschhorn, M. Lucke, S. Odenbach, Experimental and theoretical investigations on Taylor-Couette flow of ferrofluids subject to magnetic fields, *Physics Procedia* 9 (2010) 121–125. 12th International Conference on Magnetic Fluids ICMF12, 1 - 5 Aug 2010, Sendai, Japan.

[24] N. Nguyen, Z. Wu, X. Huang, C. Wen, The application of  $\mu$ PIV technique in the study of magnetic flows in a micro-channel, *Journal of Magnetism and Magnetic Materials* 289 (2005) 396–398.

[25] M. S. Krakov, I. V. Nikiforov, Thermomagnetic convection in

- a porous enclosure in the presence of outer uniform magnetic field, *Journal of Magnetism and Magnetic Materials* 289 (2005) 278–280.
- [26] T. Bednarz, E. Fornalik, T. Tagawa, H. Ozoe, J. S. Szmyd, Experimental and numerical analyses of magnetic convection of paramagnetic fluid in a cube heated and cooled from opposing verticals walls, *International Journal of Thermal Sciences* 44 (2005) 933 – 943.
- [27] T. Bednarz, E. Fornalik, H. Ozoe, J. S. Szmyd, J. C. Patterson, C. Lei, Influence of a horizontal magnetic field on the natural convection of paramagnetic fluid in a cube heated and cooled from two vertical side walls, *International Journal of Thermal Sciences* 47 (2008) 668 – 679.
- [28] T. P. Bednarz, C. Lei, J. C. Patterson, H. Ozoe, Effects of a transverse, horizontal magnetic field on natural convection of a paramagnetic fluid in a cube, *International Journal of Thermal Sciences* 48 (2009) 26 – 33.
- [29] C.-W. Wen, W.-P. Shu, Natural convection of magnetic fluid in a rectangular Hele-Shaw cell, *Journal of Magnetism and Magnetic Materials* 289 (2005) 299–302.
- [30] C.-W. Wen, W.-P. Shu, Natural convection of magnetic fluid in a rectangular Hele-Shaw cell of different aspect ratios, *Physics Procedia* 9 (2010) 181–185. 12th International Conference on Magnetic Fluids ICMF12, 1 - 5 Aug 2010, Sendai, Japan.
- [31] T. von Larcher, C. Egbers, Experiments on transitions of baroclinic waves in a differentially heated rotating annulus, *Nonlinear Processes in Geophysics* 12 (2005) 1033–1041.
- [32] A. F. Pshenichnikov, V. Mekhononshin, Equilibrium magnetization and microstructure of the system of superparamagnetic interacting particles: numerical simulation, *Journal of Magnetism and Magnetic Materials* 213 (2000) 357–369.
- [33] D. J. Tritton, *Physical Fluid Dynamics*, Oxford Science Publ, Clarendon Press, 1988.
- [34] T. Tynjälä, Theoretical and numerical study of thermomagnetic convection in magnetic fluids, Thesis, Department of Energy and Environmental Technology, Lappeenranta University of Technology, Lappeenranta, 2005.
- [35] H. W. Müller, A. Engel, Dissipation in ferrofluids: Mesoscopic versus hydrodynamic theory, *Phys. Rev.* 60 (1999) 7001–9.
- [36] K. Khanafer, K. Vafai, M. Lightstone, Buoyancy-driven heat transfer enhancement in a two dimensional enclosure utilizing nanofluid, *International Journal of Heat and Mass Transfer* 46 (2003) 3639–53.
- [37] A. Einstein, *Investigation of the theory of the Brownian movement*, Dover Publications, New York, 1956.
- [38] FLIR ®, DATA Sheet FLIR T620bx, 2016.
- [39] COMSOL Multiphysics ®, User's Guide, Version 4.4, 2013.